PNAS Nexus, 2023, 2, 1–9
https://doi.org/10.1093/pnasnexus/pgad162
Advance access publication 17 May 2023
Research Report

Cholesterol twists the transmembrane Di-Gly region of amyloid-precursor protein

David Tzu-Wei Wang[a,b], Tiffany Y.-C. Tang[a], Chun-Ting Kuo[a,b], Yun-Ting Yu[a,b], Eric H.-L. Chen[a], Ming-Tao Lee[c,d], Ruei-Fong Tsai[e], Hung-Ying Chen[e], Yun-Wei Chiang[e,*] and Rita P.-Y. Chen[a,b,f,*]

[a]Institute of Biological Chemistry, Academia Sinica, Taipei 11529, Taiwan
[b]Institute of Biochemical Sciences, National Taiwan University, Taipei 10617, Taiwan
[c]Life Science Group, Scientific Research Division, National Synchrotron Radiation Research Center, Hsinchu 30076, Taiwan
[d]Department of Physics, National Central University, Zhongli 320317, Taiwan
[e]Department of Chemistry, National Tsing Hua University, Hsinchu 300044, Taiwan
[f]Neuroscience Program of Academia Sinica, Taipei 11529, Taiwan
*To whom correspondence should be addressed: Email: pyc@gate.sinica.edu.tw; ywchiang@mx.nthu.edu.tw
Edited By: Andrey Abramov

Abstract

Nearly 95% of Alzheimer's disease (AD) occurs sporadically without genetic linkage. Aging, hypertension, high cholesterol content, and diabetes are known nongenomic risk factors of AD. Aggregation of Aβ peptides is an initial event of AD pathogenesis. Aβ peptides are catabolic products of a type I membrane protein called amyloid precursor protein (APP). Aβ40 is the major product, whereas the 2-residue-longer version, Aβ42, induces amyloid plaque formation in the AD brain. Since cholesterol content is one risk factor for sporadic AD, we aimed to explore whether cholesterol in the membrane affects the structure of the APP transmembrane region, thereby modulating the γ-secretase cutting behavior. Here, we synthesized several peptides containing the APP transmembrane region (sequence 693–726, corresponding to the $A\beta_{22-55}$ sequence) with one or two Cys mutations for spin labeling. We performed three electron spin resonance experiments to examine the structural changes of the peptides in liposomes composed of dioleoyl phosphatidylcholine and different cholesterol content. Our results show that cholesterol increases membrane thickness by 10% and peptide length accordingly. We identified that the di-glycine region of $A\beta_{36-40}$ (sequence VGGVV) exhibits the most profound change in response to cholesterol compared with other segments, explaining how the presence of cholesterol affects the γ-secretase cutting site. This study provides spectroscopic evidence showing how cholesterol modulates the structure of the APP transmembrane region in a lipid bilayer.

Keywords: cholesterol, Alzheimer's disease, amyloid precursor protein, Aβ, transmembrane helix, electron spin resonance spectroscopy, lamellar X-ray diffraction, orientated circular dichroism spectroscopy

Significance Statement

Cholesterol content is one risk factor for sporadic Alzheimer's disease (AD). The Aβ42/Aβ40 ratio is determined by the cutting reaction of γ-secretase on the transmembrane helix of amyloid precursor protein (APP) and affects the AD onset age. Here, we used electron spin resonance spectroscopy to examine changes in the local structure of the APP transmembrane region in response to cholesterol content in the dioleoyl phosphatidylcholine vesicles. We found that cholesterol increased the length of the APP transmembrane helix and, most importantly, affected the helical backbone orientation of the di-Gly region above the Aβ40 cutting site. The new information provides an improved understanding of the cholesterol-sensitive region in the APP transmembrane helix.

Introduction

According to the World Health Organization (https://www.who.int/health-topics/dementia#tab=tab_2), around 50 million people worldwide have dementia, a number that is expected to rise to over 100 million in 2050, being a healthcare burden and substantially impacting society. About 60–70% of dementia patients are diagnosed with Alzheimer's disease (AD). Despite the efforts of >100 years, AD is incurable and irreversible. Delaying AD onset for 5 years can result in a 41% lower prevalence and 40% lower cost by 2050 (1). Current strategies for AD prevention include the identification of risk factors and early detection of pathophysiological hallmarks, so that the risk of acquiring AD could be reduced by nutritional counseling, lifestyle changes, and early treatment. The deposition of senile plaques in the patient's brain is the initial event in AD progression. The main components in the senile plaques are amyloid-beta (Aβ) peptides, including Aβ40 of the major

Competing Interest: The authors declare no competing interest.
Received: February 6, 2023. **Accepted:** May 8, 2023

component and Aβ42 of the more toxic component, which are the catabolic products of amyloid precursor protein (APP) by β-secretase and γ-secretase. The ratio of Aβ42/Aβ40 is correlated to the patients' onset age (2). The early-onset patients have genetic mutations in APP or secretases. On the other hand, late-onset AD is sporadic, and the apolipoprotein E (apoE) ϵ4 allele has been identified as the biggest genetic risk factor for sporadic AD (3, 4).

The brain is the most cholesterol-rich organ in the body. The central nervous system contains ∼25% of total cholesterol (5). Apolipoprotein E is critical for cholesterol metabolism in the brain and transports cholesterol and other lipids between neurons and glial cells (6, 7). The principal site of Aβ production in the cell is the cholesterol-rich membrane areas (lipid rafts) (8, 9). Rabbits fed a 2% cholesterol diet showed extracellular Aβ amyloid deposits in the cortex, and the accumulation amount was correlated with the feeding duration (10). Hypercholesterolemic mice increased β-amyloid load, especially Aβ42 (11). In contrast, Aβ accumulation was reduced in AD transgenic mice treated with cholesterol-lowering drugs (12, 13). Several epidemiology studies have implicated an elevated serum cholesterol level (specifically, a low-density lipoprotein cholesterol level) as a risk factor for AD (14–17). Patients receiving lovastatin or pravastatin (HMG-CoA reductase inhibitors that decrease cholesterol production) had a lower prevalence of probable AD (18). It is controversial whether cholesterol could affect Aβ production via its effect on γ-secretase. Using the in vitro assays, some studies have claimed that γ-secretase activity is cholesterol-dependent (9, 19, 20), while some studies did not find the correlation (21). To sum up, excessive cholesterol accumulation in the brain is a risk factor for dementia (22) and is related to several AD-associated pathologies (23, 24).

Cholesterol in the membrane plays an important role in Aβ production and aggregation. Still, very few studies have explored whether the structure of the APP membrane-spanning region is affected by the induction of cholesterol. There are two groups studying the structure of the APP transmembrane region in micelles using NMR spectroscopy. Nadezhdin et al. incorporated an isotope-labeled $APP_{686–726}$ fragment (corresponding to $Aβ_{15–55}$) in dodecyl phosphocholine (DPC) micelles (25). They found two perpendicular α-helices formed in DPC micelles. The shorter helix, corresponding to $Aβ_{16–23}$, lies in the region of hydrated polar DPC groups. The longer helix, corresponding to the membrane-spanning region $Aβ_{29–52}$, transpierces the hydrophobic part of the micelles. By adding cholesteryl hemisuccinate to the micelles, only residues of Gly-25, Ser-26, Gly-29, Ile-32, and Gly-33 had a significant change in the chemical shift of the amide proton. Another study by Barrett et al. incorporated an APP catabolic fragment called C99 into the myristoyl phosphatidylglycerol micelles (26). They reported that the structure of the transmembrane region ($Aβ_{29–52}$) is a curved α-helix in which the two adjacent glycine residues, Gly-37 and Gly-38, form a G-G kink in the apex of the curvature. Substituting residues Gly-29, Ile-32, Gly-33, and Val-40 by Ala affected cholesterol binding. These two studies used different APP fragments and lipids. They yielded different structural results, but both found cholesterol binding at the GXXXG motif.

In this study, we were interested in studying whether cholesterol could affect the transmembrane region of APP by means of electron spin resonance (ESR) spectroscopy. The experimental protocol is shown in Fig. 1. Briefly, we synthesized cysteine variants of peptides containing the sequence of the APP membrane-spanning region. The peptides were embedded in liposomes composed of dioleoyl phosphatidylcholine (DOPC) and different amounts of cholesterol. Three different ESR experiments were then performed to identify cholesterol-induced structural changes in the transmembrane peptides. The ESR experiments performed included continuous-wave ESR (CW-ESR), double electron–electron resonance (DEER), and electron spin echo envelope modulation (ESEEM).

Results and discussion

Cholesterol promotes an extended helical model in the APP transmembrane region

The two ends of the APP transmembrane region are fixed to the lipid bilayer border by positively charged Lys-28 at the N-terminus and Lys-53, Lys-54, and Lys-55 at the C-terminus. Due to the hydrophobic nature of the lipid bilayer, there are many hydrophobic residues in the APP transmembrane region. However, it is worth noting that four glycine residues (Gly-29, Gly-33, Gly-37, and Gly-38) are in the transmembrane region's upper part. Glycine is known as a "helix breaker." Moreover, Nadezhdin et al. have reported that this Gly-rich region happens to be the cholesterol-binding site (25). Here, we chose Gly-29 and Ile-47 to be spin-labeling sites, because the 29–47 region covers the whole membrane-spanning region of the Aβ peptides and the γ-secretase cutting site. This region contains five helical turns, and the estimated spin–spin distance is ∼2.7 nm and within the detection range of DEER ESR spectroscopy (1.5–6 nm).

We synthesized a peptide named KKWK-$Aβ_{22–55}$-G29C/I47C, which contains the "KKWK" sequence for increasing peptide solubility and for peptide quantification. The Gly-29 and Ile-47 of $Aβ_{22–55}$ were mutated to Cys (Fig. 2a) to prepare the double-labeled peptide encoded as 29/47R1. The 29/47R1 was embedded in DOPC liposomes containing 0, 10, and 15% (w/w) cholesterol. Their circular dichroism (CD) spectra confirmed that the peptides adopt an α-helical structure in the liposomes (Fig. S1). The orientated CD (OCD) spectra proved that these peptides were inserted into the lipid bilayers (Fig. S2). Hutchison et al. have reported that the C99 protein (the C-terminal catabolic product of APP after β-secretase cleavage) embedded in the sphingomyelin and cholesterol-rich DMPC-based bicelles formed a mixture of monomer, dimer, and trimer (27). Song et al. showed that dimerization and cholesterol binding is a competitive process (28). To ensure our peptides are monomeric in the liposomes, the CW-ESR spectra of single-labeled peptides in the liposomes composed of different peptide: lipid ratios were recorded. No peak broadening was found in the liposome of 1:300 (peptide:lipid) mixing ratio, suggesting that our peptides do not associate under this condition.

Using DEER spectroscopy, the distance distribution of the 29/47R1 in the DOPC liposome without cholesterol displayed one primary population at 2.5 nm (Fig. 2b and c). The distances corresponding to the 29/47R1 in 10 and 15% cholesterol liposomes shifted clearly to longer distances (2.7–2.8 nm), indicating that the presence of cholesterol affects the local structure and promotes an increase in the helix length. The structure of the APP membrane-spanning region is more similar to the simulated distance distribution based on the 2LLM model, as opposed to the 2LP1 model, suggesting that there is no bending in the middle of our transmembrane helix in the DOPC lipid bilayer. The all-atom molecular dynamic simulation data done by Lemmin et al. also supported the straight helix model (29).

Changes in local segments of the peptide revealed by CW-ESR

The DEER data suggested that the content of cholesterol affected the helical structure. Furthermore, we used CW-ESR to explore

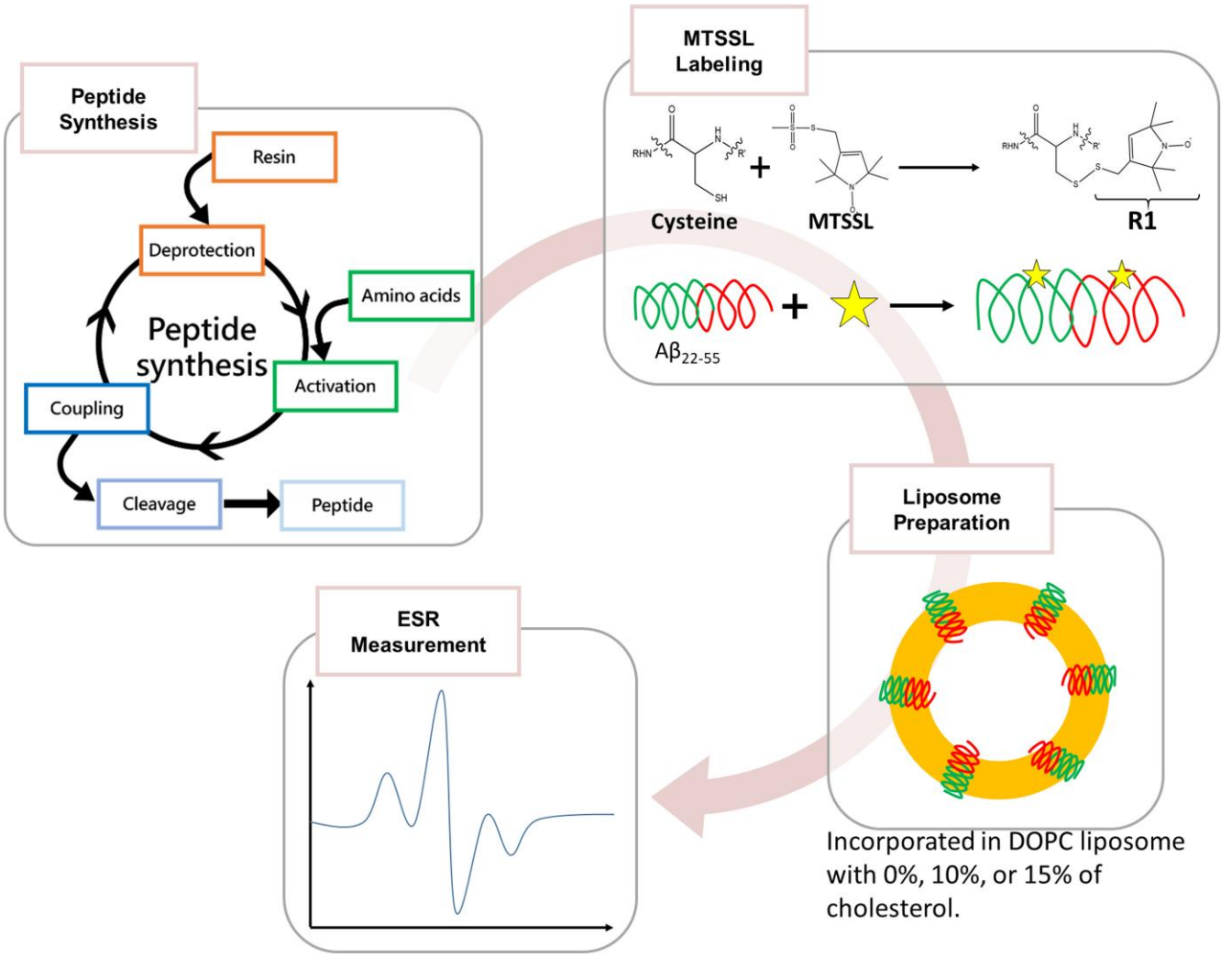

Fig. 1. The experimental protocol to study the cholesterol-induced difference in the transmembrane region of APP by ESR.

which segment was affected by cholesterol. We selected $A\beta_{29–36}$, $A\beta_{29–40}$, and $A\beta_{40–47}$ as our target segments (Fig. 3a). The interspin distances predicted from the model (PDB ID: 2LLM) in the double-labeled peptides 29/36R1, 29/40R1, and 40/47R1 (Fig. 3b) were 1.3, 1.6, and 1.4 nm, respectively. The CW-ESR spectra corresponding to the double- (red line) and single-labeled (blue line) peptides were recorded. The experimental spectra are presented in the normalized absorption mode to emphasize the changes in linewidth broadening (highlighted by dotted boxes in Fig. 3c) with labeling sites. The CW-ESR is sensitive to interspin distances <2 nm. The shorter the interspin distances, the greater the linewidth broadening in the double-labeled spectrum (denoted by *D*), as compared with the sum of the single-labeled spectra (denoted by *S*). Our results (Fig. 3c) show that the extent of the linewidth broadening was in this order: 29/36R1 > 40/47R1 > 29/40R1.

Figure 3d shows the interspin distance distributions extracted from the CW-ESR spectra using the Tikhonov-based method (30). The average distances and the FWHM values are ~1.21 ± 0.1 (29/36R1), 1.36 ± 0.1 (40/47R1), and 1.65 ± 0.3 (29/40R1) nm, consistent with the trend of linewidth broadening obtained from the visual inspection of the experimental spectra (Fig. 3c). A comparison of the ESR-derived distances and the predictions from the NMR model (indicated by red dash lines in Fig. 3d) revealed that the presence of cholesterol primarily causes a change in segment 29/40R1. Little change was observed for the 29/36R1 and 40/47R1 in response to cholesterol. Moreover, in Fig. 3d, 29/40R1 had increased peak width upon cholesterol addition, whereas 29/36R1 did not, suggesting that the 36–40 segment is the source of increased structural flexibility. Taken together, the data suggest that cholesterol exerts the most profound influence on the 36–40 segment. The 36–40 segment may be somewhat rotated or twisted in response to cholesterol.

ESEEM to verify the local difference in the Gly_{37}–Gly_{38} region

The $A\beta_{36–40}$ region contains two consecutive Gly residues (Gly_{37}–Gly_{38}). Without the restraint of the side chain, Gly could provide high flexibility to the conformer of the polypeptide chain. To identify cholesterol-induced changes in the helical structure of the APP peptide by means of the pulse ESEEM technique, we prepared variants of the peptide by fixing ^{2}H-labeled Val (d_8) at position 36 (*i*) and varying the MTSSL spin label at two different positions (*i* + 3 and *i* + 4). The two peptides are denoted by V36d_8-V39R1 and V36d_8-V40R1 (Fig. 4a). The three-pulse ESEEM technique was utilized to detect the weakly coupled interactions between the ^{2}H atoms on the Val side chain and the MTSSL nitroxide probe, following the previously established ESEEM-based strategy for

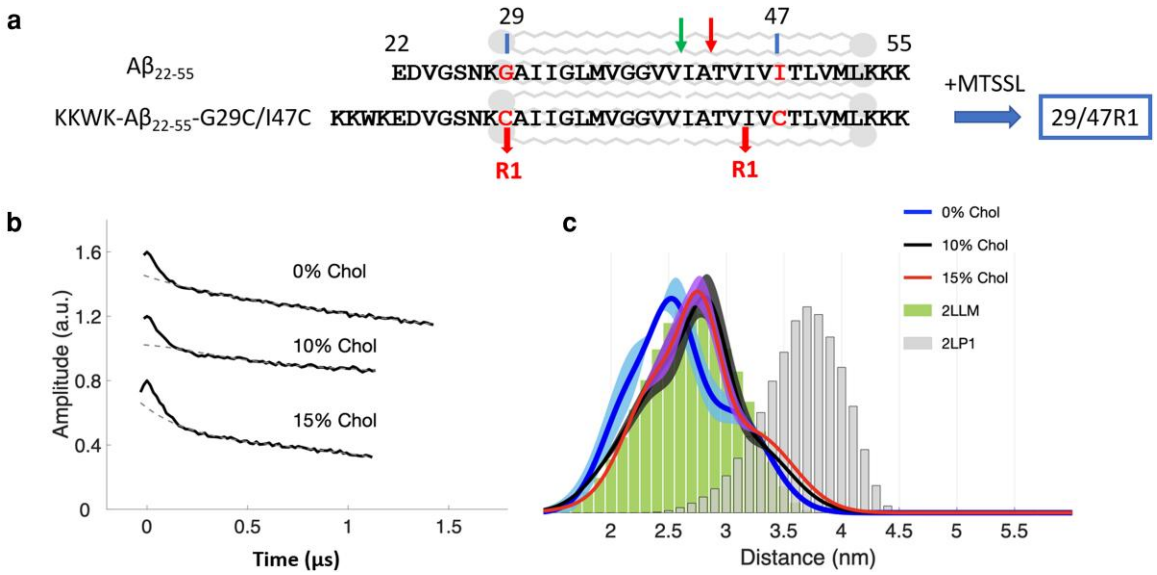

Fig. 2. The DEER measurements on the 29/47R1. a) Peptide sequence and spin-labeling sites. The arrows mark the γ-secretase cutting sites for producing Aβ40 (left arrow) and Aβ42 (right arrow). The membrane region is marked. b) Dipolar time evolution data from the DEER measurements of the 29/47R1 in the DOPC liposomes, containing 0, 10, and 15% (w/w) cholesterol. c) Interspin distance distributions of the 29/47R1 extracted from the DEER data. The shading around the lines represents uncertainty bounds. The distance distributions predicted from the structure models reported by Nadezhdin et al. (PDB: 2LLM) and Barrett et al. (PDB: 2LP1) are displayed by bar plots (25, 26).

distinguishing between the structures of α-helix and 3_{10}-helix (31). We performed the ESEEM measurements on the two samples in DOPC liposomes containing different contents of cholesterol at 0, 10, and 15%. The time-domain ESEEM data (Fig. 4b) of the $i+4$ ($V36d_8$-V40R1) samples exhibit a distinct damped oscillation compared with the data of the $i+3$ ($V36d_8$-V39R1) samples. The distinct difference in the time-domain ESEEM data indicates that the distances between the side chains of the i and $i+4$ positions are within the ESEEM sensitivity range (~0.8 nm), while the distances between i and $i+3$ are outside the detection limit.

After Fourier transforming the time-domain data, we observed that a distinct ^{2}H Larmor frequency (~2.2 MHz) appears only in the frequency-domain ESEEM data for $i+4$ (Fig. 4c). The peaks for 10 and 15% cholesterol are similar in intensity (1.60 and 1.42, respectively), which are ~1.5 times the peak intensity for 0% cholesterol. The greater peak intensity was strong evidence that the side chains of the i and $i+4$ positions pointed toward the same side of the helix in 10 and 15% cholesterol; they were closer in proximity compared with that in 0% cholesterol. Our data suggest that the presence of cholesterol twists the local region containing V36 and V40, and promotes consistency in the orientation of the two residues, as the distance between V36R1 and V40R1 in 10% cholesterol was the shortest among all studied. In addition, the data support that $Aβ_{36–40}$ forms an α-helical structure rather than a 3_{10}-helix in the DOPC bilayer.

Previous NMR studies have reported two different structural models of APP peptides in micelles (Fig. 4d); their PDB codes are 2LP1 and 2LLM, where the former is characterized by a kink and is highly curved compared with the latter. As illustrated, the side chains of i and $i+3$ point toward the same side in 2LP1, whereas the side chains of i and $i+4$ are aligned along the same side in 2LLM. Our ESEEM results indicate that, in a DOPC lipid environment, the APP peptide forms an α-helix structure similar to 2LLM, and the helix is twisted in the presence of cholesterol (Fig. 4e).

Barrett et al. have studied the distance between Gly-29 and Leu-52 in the POPG/POPC liposomes using DEER spectroscopy (26). They found that replacing Gly-37 or Gly-38 with Leu reduced the structural flexibility of the transmembrane helix of C99. This finding provides a good explanation for our results. We found that when the two ends of the APP transmembrane region are fixed to the membrane borders by Lys-28 and Lys-53, the di-Gly region provides structural flexibility upon cholesterol-induced membrane thickening.

Thickness of the DOPC lipid bilayer with or without cholesterol

Gallová et al. reported that cholesterol addition did not change the lipid thickness of the DOPC bilayer in unilamellar vesicles but increased the thickness of the dilauroyl phosphatidylcholine bilayer from 4.058 to 4.62 nm by the small-angle neutron scattering technique (32). The membrane thickening effect of cholesterol in multilayered lipids has been reported previously (33). In this study, we used lamellar X-ray diffraction (LXD) to examine the lipid thickness in the DOPC multilayers, with or without cholesterol. The obtained LXD diffraction patterns are shown in Fig. S3, and the repeating distances (D) in the lipid multilayers were calculated from the angle of the diffraction peaks. Figure 5 shows the transbilayer electron density profiles of different lipid multilayers. The distance between the two maximums indicated by vertical bars in this figure is the bilayer thickness, which is also called the phosphate-to-phosphate (ptp) distance. The thickness of the water layer (Dw) between the lipid bilayers was calculated by deducting the bilayer thickness from the repeating distances in the lipid multilayers.

The LXD results are summarized in Table 1. The thicknesses of the DOPC and DOPC+ 15% cholesterol bilayers were 3.68 and 4.09 nm, respectively. Cholesterol increased the membrane thickness by 0.4 nm. The bilayers of the DOPC+ 15% cholesterol with and without peptide maintained the same thickness of 4.09 nm, suggesting that peptide insertion does not increase the membrane thickness. Our DEER and CW-ESR showed that the peptide length

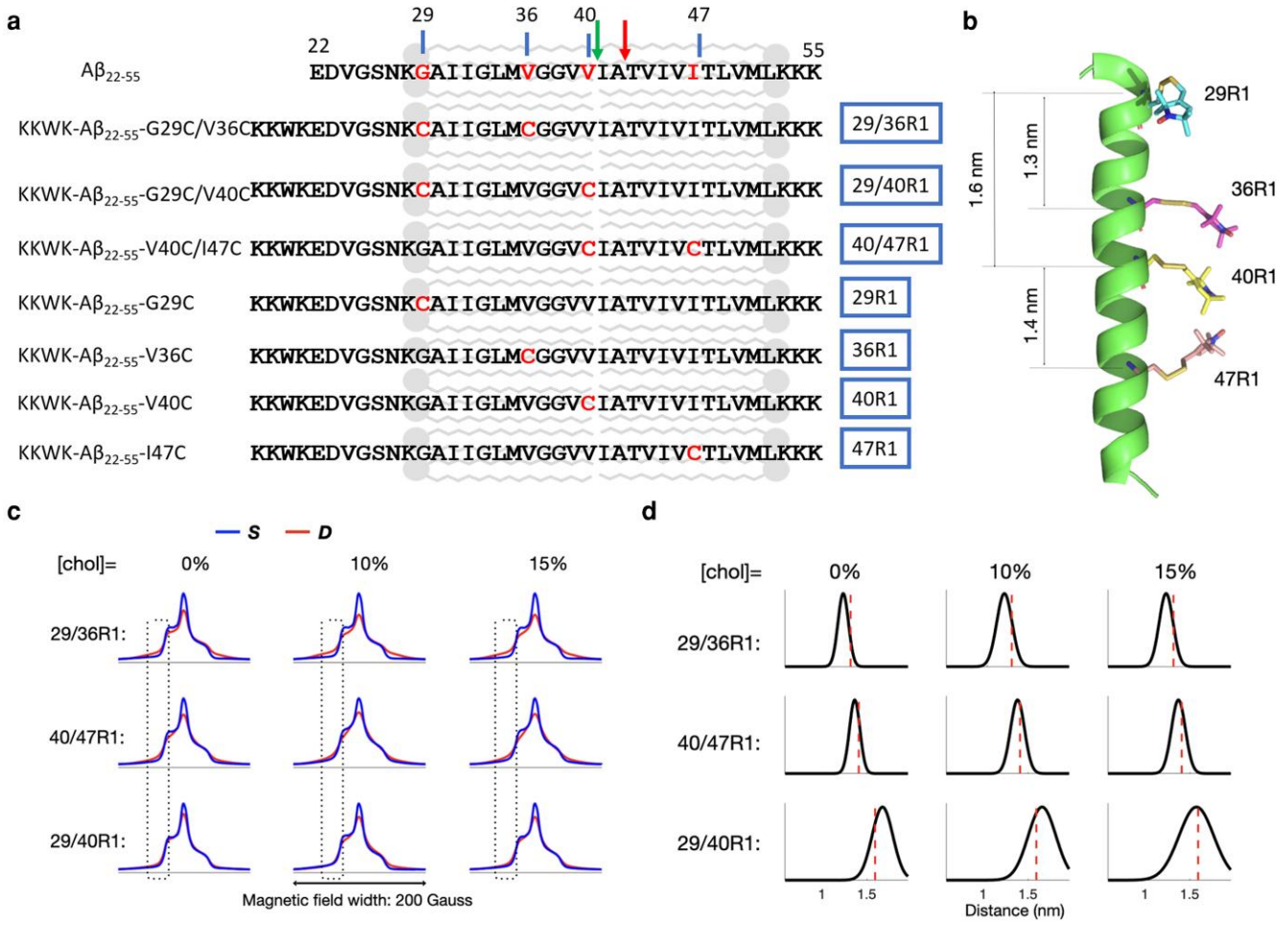

Fig. 3. The CW-ESR results. a) Sequences and spin-labeling sites of the peptides used. The arrows mark the γ-secretase cutting sites for producing Aβ40 (left arrow) and Aβ42 (right arrow). The membrane region is marked. b) Average interspin distances predicted from the 2LLM model using the mtsslWizard program. c) The CW-ESR spectra displayed in the normalized absorption mode. They are samples of 29/36R1, 29/40R1, and 40/47R1 embedded in DOPC liposomes containing 0, 10, and 15% cholesterol. d) Interspin distance distributions extracted from the CW-ESR spectra. The dashed lines correspond with the predicted distances, as shown in b.

increased as the membrane thickness increased, and that the change mainly occurred in the Gly-rich segment above the γ-secretase cutting sites. On the other hand, the water layer thickness of DOPC+ 15% cholesterol with peptide is 1.67 nm, which is larger than that without peptide (1.40 nm). Because the N-terminus of our peptide contains 10 residues that were not in the membrane-spanning region, the increased Dw thickness might have resulted from this membrane-exposed polypeptide chain.

Conclusion

In this study, we employed three ESR experiments to investigate how cholesterol affects the structure of the membrane-spanning region of the APP. We found that the peptide containing the sequence corresponding to this region adopts a straight α-helical structure in DOPC liposomes. However, when cholesterol was added to the liposomes, the lipid thickness increased, and the backbone of the di-Gly region was twisted, causing the helix length to increase. Notably, the di-Gly region is located above the Aβ40 cutting site, so changing the side-chain orientation could impact the choice of the γ-secretase cutting site.

Materials and methods

Peptide synthesis

All mutated APP transmembrane helix series were synthesized by solid-phase peptide synthesis on a PS3 peptide synthesizer (Protein Technologies, Inc., AZ, USA) following a modified protocol in the literatures (34, 35). The Fmoc-Lys(Boc)-Wang resin (0.1 mmol) was used as the solid support. Thirty percent of piperidine in dimethylformamide (DMF, v/v) was used to remove the protecting Fmoc group. The activation solution (4.45% *N*-methylmorpholine [NMM], 25% DMSO in DMF, v/v) was used to dissolve 0.6 mmol of Fmoc-protected amino acid and equal molar *O*-(benzotriazol-1-yl)-*N*,*N*,*N*′,*N*′-tetramethyluronium hexafluorophosphate in the amino acid vial. Then, the mixture was injected into the reaction vessel for 3 or 6 h to complete one synthesis cycle. After the peptide synthesis was completed, 10 mL of cleavage cocktail (trifluoroacetic acid/water/ethanedithiol 95/2.5/2.5% v/v/v) was reacted with the resin by stirring at room temperature for 2 h to deprotect the side chains and cleave the peptide from the resin. The resin was then removed by filtration, and the peptide in the filtrate was precipitated by adding 10 volumes of ice-cold methyl *t*-butyl ether (MTBE). The precipitate was collected by centrifugation at 3,000 *g* for 15 min at 4°C,

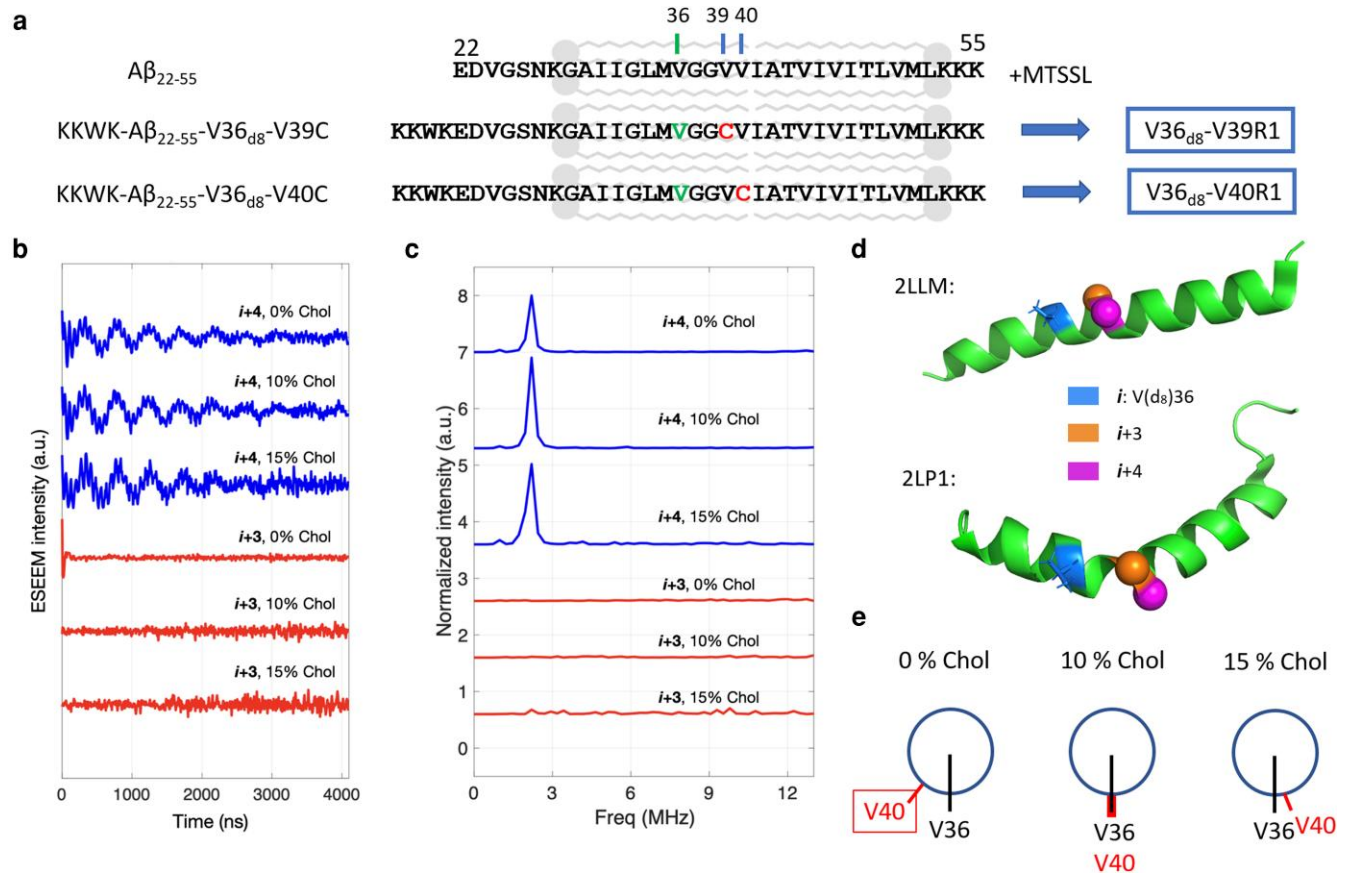

Fig. 4. The ESEEM results of V36d_8-V39R1 and V36d_8-V40R1. a) Sequences and spin-labeling sites of the peptides used. The membrane region is marked. b) Time-domain ESEEM spectra of the peptides with a deuterated Val at position *i*, a nitroxide spin-labeled at *i* + 4 (V36d_8-V40R1, blue), and *i* + 3 (V36d_8-V39R1, red) samples at 0, 10, and 15% cholesterol. c) Fourier-transformed ESEEM spectra. A distinct ^{2}H Larmor frequency (~2.2 MHz) appears in the *i* + 4 samples. d) Previously reported structural models of the APP peptide in micelles. Their PDB codes are noted. e) The surmised illustration of the relative orientation of Val-36 and Val-40 in the presence of different cholesterol concentrations.

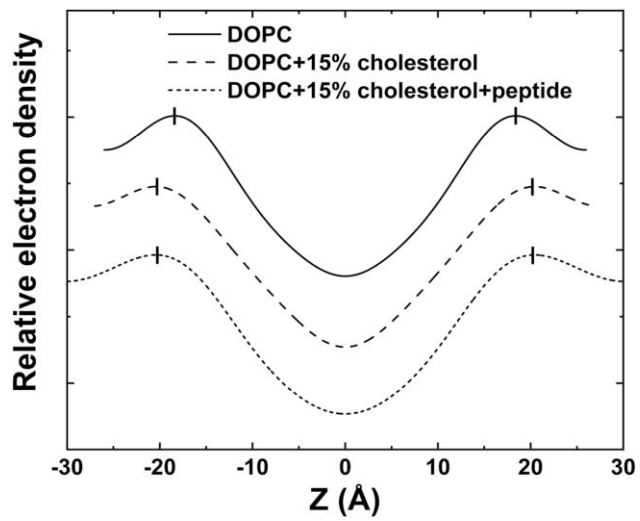

Fig. 5. The electron density profiles of DOPC, DOPC+ 15% cholesterol, and DOPC+ 15% cholesterol + peptide at 98.5% relative humidity and 30°C. The profiles were not normalized and were displaced for clarity. The short vertical bars indicate the positions of the peaks. The distance between the vertical bars is the ptp distance.

Table 1. Structural parameters of lipid bilayers determined by LXD at 98.5% relative humidity and 30°C.

Sample	*D* (nm)	ptp (nm)	Dw (nm)
DOPC	5.17	3.68	1.49
DOPC+ 15% cholesterol	5.49	4.09	1.40
DOPC+ 5% cholesterol + peptide	5.76	4.09	1.67

The repeating distance (*D*) was calculated from the angle of the diffraction peaks in Fig. S3 by Bragg's law. The ptp distance, defined as bilayer thickness, was extracted from the electron density pattern. The thickness of the water layer (Dw) between bilayers was obtained as follows: *D* = ptp + Dw.

washed twice with ice-cold MTBE, and dried under vacuum to obtain the crude peptide.

MTSSL labeling of peptides and purification

The crude peptide was dissolved in DMSO and quantified by absorbance at 280 nm. Then, the (1-oxyl-2,2,5,5-tetramethyl-3-pyrroline-3-methyl)methanethiol-sulfonate (MTSSL; Enzo Life Sciences, Taiwan) stock solution (126 mM in DMSO) and activation solution (4.45% NMM, 25% DMSO in DMF, v/v) were mixed with the peptide (molar ratio of peptide:MTSSL:NMM = 1:3:5).

The reaction was conducted in the dark at room temperature for 2.5 h, after which the solvent was removed by lyophilization.

The labeled peptide was dissolved in 20% trifluoroethanol. The premature peptides and unreacted MTSSL were removed using the 3,000 Dalton Ultra Centrifugal Filter (Merck, Taiwan) at 2,500 *g* for 45 min at 4°C. Next, the concentrated solution was applied to a PD-10 column (GE, USA) to collect the purified peptide. The purified peptide was lyophilized and stored at −30°C. The quality of the peptide was checked using MALDI-TOF mass spectroscopy.

Liposome preparation

The DOPC (Avanti) and the cholesterol (Sigma-Aldrich) were dissolved in a freshly premixed mixture of hexafluoroisopropanol (HFIP) and chloroform (3:1, v/v) to the concentrations of 10 and 5 mg/mL, respectively. The labeled peptide was also dissolved in the same solvent cocktail. Then, 50 nmol peptide and 15,000 nmol lipids were mixed (P/L ratio, 1:300) by vortex, then the solvent was evaporated using an N_2 purge with a gentle vortex. The lipid film formed layer by layer on the wall of an Eppendorf tube. The tube was placed in a vacuum chamber overnight.

About 750 μL of phosphate buffer (10 mM PB, 50 mM NaCl, pH 7) was added to the lipid film and mixed mildly using a rotary device (Intelli mixer, ELMI, Latvia) at 10 rpm for 20 min. Then, the solution was alternatively placed in a 50°C water bath and liquid nitrogen for five freeze-thaw cycles (5 min each). Finally, the solution was extruded through a polycarbonate filter (with a 200-nm pore size) using the Avanti Mini-Extruder (Avanti Polar Lipids, USA) to prepare the liposomes. The liposomes were stored in a 4°C fridge. For ESR measurement, glycerol was added to the liposomes to a final concentration of 20%.

CD spectroscopy

The embedded peptide in the liposomes was diluted five times with phosphate buffer (10 mM PB, 50 mM NaCl, pH 7). Two hundred microliters of the sample were put into a quartz cuvette with a path length of 1 mm, and the spectra were recorded two times, from 195 to 260 nm, with a scanning speed of 50 nm/min on a J-815 CD spectrometer (JASCO, Japan). The bandwidth was set to 1 nm, and the step resolution was 0.5 nm.

OCD spectroscopy

The KKWK-Aβ_{22-55} was mixed with DOPC, with and without cholesterol (peptide/lipid molar ratio, 1:10), in HFIP/chloroform (3/1). The final peptide concentration was 100 μM. Four microliters of the mixed sample were dropped into a sample chamber whose design was described in the literature (36). Multiple layers of lipids were formed after solvent volatilization. Ten microliters of water were added to the rim of the sample chamber to retain humidity. The OCD spectrum was recorded three times on a J-815 CD spectrometer (JASCO, Japan) from 195 to 250 nm with a scanning speed of 50 nm/min and a step resolution of 0.5 nm.

Pulsed ESR (DEER and ESEEM)

The pulsed EPR experiments were conducted at 80 K using a Bruker ELEXSYS E580-400 CW/pulsed spectrometer, with a split-ring resonator (EN4118X-MS3) and a helium gas flow system (4118CF and 411A). A liposome sample of ~40 μL, containing 20% glycerol, was transferred into a 3-mm EPR quartz tube sealed with parafilm. All samples were frozen quickly by liquid nitrogen before being inserted into the sample cavity, which was precooled to the desired temperature of 80 K (37, 38).

The DEER experiments were performed using the typical four-pulse constant-time DEER sequence as previously described (39). The interspin distance distribution was determined using time-domain analysis by Tikhonov regularization based on the L-curve method (40), followed by a data refinement process, using the maximum entropy method to obtain the nonnegative probability density (41, 42). Error estimates of the DEER distance distributions were calculated from all trials of the background correction parameters in the Tikhonov regularization analysis.

Three-pulse electron spin echo envelope modulation (ESEEM) measurements were performed with a $\pi/2$-τ-$\pi/2$-T-$\pi/2$-τ-echo pulse sequence using four-step-phase cycling (43). The pulse length of the $\pi/2$ pulses was set to 16 ns and the interpulse delay τ was 200 ns, which corresponds with a proton blind spot to suppress the proton modulations (31, 44, 45). The second interpulse delay, *T*, was set by an initial value of 386 ns, incremented by 8 ns with 512 data points, with the magnetic field strength fixed at 3,360 G. The integration gate length was 60 ns. All ESEEM data were collected at a microwave frequency of ~9.425 GHz.

Continuous-wave ESR

For the CW-ESR measurement, ~200 μL of the sample, which contained 20% glycerol, was transferred into a 4-mm EPR quartz tube. The CW-ESR spectra were recorded in a Bruker ELEXSYS 580, equipped with an X-band microwave bridge and ER 4122 SHQE resonator, and an ER 4131 VT unit for temperature control. The spectra were recorded at 200 K with a microwave frequency of ~9.43 GHz, microwave power of 1.5 mW, modulation frequency of 100 kHz, modulation amplitude of 1 G, and scan width of 200 G and 1,024 data points.

Lamellar X-ray diffraction

The LXD measurements were carried out at the Taiwan Light Source beamline BL13A1, equipped with an X-ray diffractometer and Bicron detector of the National Synchrotron Radiation Research Center, Taiwan. The oriented multilayer sample used in the LXD measurement was a stack of parallel hydrated lipid bilayers on a solid substrate. The preparation of such oriented samples followed the method described in previous studies (46, 47). One milligram of lipid sample was premixed and dissolved in 20 μL of HFIP/chloroform mixture (3/1). For the samples containing peptide, the molar ratio of peptide to lipid was 1:20. Ten microliters of the sample were spread onto a cleaned silicon wafer surface of 22 mm × 14 mm (L × W). After the solvents evaporated and the sample dried, the sample was vacuumed to remove the residual solvents and then slowly hydrated at high relative humidity until it appeared transparent.

The oriented samples were loaded into a temperature-humidity controlled chamber for LXD measurements. The temperature was set at 30°C. In addition to the measurement at 98.5% relative humidity (RH), the measurements were performed at lower humidity levels for the determining phase. A precise RH reading for these lower levels of humidity was not necessary because the phase determination via the swelling method may use the repeat distances as the variables (48, 49). The equilibrium of the sample at each humidity level was ensured by an agreement of two subsequently analyzed diffraction patterns. The data reduction of LXD was described previously (47, 50). Briefly, it started with a background removal of diffraction patterns in Fig. S3, followed by absorption and diffraction volume corrections. Subsequently, the integrated areas of diffraction peaks in Fig. S3 were corrected for polarization and Lorentz factors (48). The

magnitude of the scattering amplitude was the square root of the integrated intensity. The phases were determined by the swelling method (Fig. S4) (48, 49). With their phases determined, the scattering amplitudes were Fourier-transformed to obtain the relative trans-bilayer electron density profiles in Fig. 5. Instead of normalization to the absolute scale, the profiles gave the correct ptp distances, which are independent of the normalization (51).

Acknowledgments

The authors thank Ms. Hsi-Lin Cheng for the mass identification of our peptide in the Mass Spectrometer Facility at the Institute of Molecular Biology of Academia Sinica. The CD and OCD spectra were recorded in the Biophysical Instrumentation Laboratory at the Institute of Biological Chemistry of Academia Sinica. All ESR measurements were conducted at the Research Instrument Center of Taiwan, located at NTHU.

Supplementary material

Supplementary material is available at *PNAS Nexus* online.

Funding

This work was supported by Academia Sinica and the National Science and Technology Council of Taiwan (grant no.: MOST 110-2113-M-001-030; 111-2113-M-001-048 to R.P.Y.C.; 111-2113-M-007-015 to Y.-W.C.).

Author contributions

R.P.-Y.C. designed the research and analyzed data; D.T.-W.W., T.Y.-C.T., C.-T.K., Y.-T.Y., E.H.-L.C., R.-F.T., and H.-Y.C. performed research; M.-T.L. provided instruments and analyzed the LXD data; Y.-W.C. provided instruments and analyzed the ESR data; M.-T.L., Y.-W.C., and R.P.-Y.C. wrote the paper.

Data availability

All data needed to evaluate the study are present in the paper or the Supplementary Material.

References

1 Zissimopoulos J, Crimmins E, St. Clair P. 2014. The value of delaying Alzheimer's disease onset. *Forum Health Econ Policy*. 18(1): 25–39.
2 Bateman RJ, *et al.* 2012. Clinical and biomarker changes in dominantly inherited Alzheimer's disease. *N Engl J Med*. 367(9): 795–804.
3 Kivipelto M, *et al.* 2002. Apolipoprotein E epsilon4 allele, elevated midlife total cholesterol level, and high midlife systolic blood pressure are independent risk factors for late-life Alzheimer disease. *Ann Intern Med*. 137(3):149–155.
4 Piaceri I, Nacmias B, Sorbi S. 2013. Genetics of familial and sporadic Alzheimer's disease. *Front Biosci*. 5(1):167–177.
5 Martins IJ, *et al.* 2009. Cholesterol metabolism and transport in the pathogenesis of Alzheimer's disease. *J Neurochem*. 111(6): 1275–1308.
6 Kim J, Basak J, Holtzman D. 2009. The role of apolipoprotein E in Alzheimer's disease. *Neuron*. 63:287–303.
7 Dietschy J. 2009. Central nervous system: cholesterol turnover, brain development and neurodegeneration. *Biol Chem*. 390: 287–293.
8 Vetrivel KS, Thinakaran G. 2010. Membrane rafts in Alzheimer's disease beta-amyloid production. *Biochim Biophys Acta*. 1801(8): 860–867.
9 Wahrle S, *et al.* 2002. Cholesterol-dependent γ-secretase activity in buoyant cholesterol-rich membrane microdomains. *Neurobiol Dis*. 9:11–23.
10 Sparks DL, *et al.* 1994. Induction of Alzheimer-like β-amyloid immunoreactivity in the brains of rabbits with dietary cholesterol. *Exp Neurol*. 126(1):88–94.
11 Refolo LM, *et al.* 2000. Hypercholesterolemia accelerates the Alzheimer's amyloid pathology in a transgenic mouse model. *Neurobiol Dis*. 7(4):321–331.
12 Refolo LM, *et al.* 2001. A cholesterol-lowering drug reduces β-amyloid pathology in a transgenic mouse model of Alzheimer's disease. *Neurobiol Dis*. 8(5):890–899.
13 Fassbender K, *et al.* 2001. Simvastatin strongly reduces levels of Alzheimer's disease β-amyloid peptides Aβ42 and Aβ40 in vitro and in vivo. *Proc Natl Acad Sci USA*. 98(10):5856–5861.
14 Kuo Y-M, *et al.* 1998. Elevated low-density lipoprotein in Alzheimer's disease correlates with brain Aβ 1–42 levels. *Biochem Biophys Res Commun*. 252(3):711–715.
15 Burns M, Duff K. 2002. Cholesterol in Alzheimer's disease and tauopathy. *Ann NY Acad Sci*. 977:367–375.
16 Launer LJ, White LR, Petrovitch H, Ross GW, Curb JD. 2001. Cholesterol and neuropathologic markers of AD: a population-based autopsy study. *Neurology*. 57(8):1447–1452.
17 Evans RM, *et al.* 2000. Serum cholesterol, APOE genotype, and the risk of Alzheimer's disease: a population-based study of African Americans. *Neurology*. 54(1):240–240.
18 Wolozin B, Kellman W, Ruosseau P, Celesia GG, Siegel G. 2000. Decreased prevalence of Alzheimer disease associated with 3-hydroxy-3-methyglutaryl coenzyme A reductase inhibitors. *Arch Neurol*. 57(10):1439–1443.
19 Simons M, *et al.* 1998. Cholesterol depletion inhibits the generation of β-amyloid in hippocampal neurons. *Proc Natl Acad Sci USA*. 95:6460–6464.
20 Buxbaum JD, Geoghagen NS, Friedhoff LT. 2001. Cholesterol depletion with physiological concentrations of a statin decreases the formation of the Alzheimer amyloid Aβ peptide. *J Alzheimers Dis*. 3(2):221–229.
21 Wada S, *et al.* 2003. Gamma-secretase activity is present in rafts but is not cholesterol-dependent. *Biochemistry*. 42(47): 13977–13986.
22 Iwagami M, *et al.* 2021. Blood cholesterol and risk of dementia in more than 1·8 million people over two decades: a retrospective cohort study. *Lancet Healthy Longev*. 2(8):e498–e506.
23 Helzner EP, *et al.* 2009. Contribution of vascular risk factors to the progression in Alzheimer disease. *Arch Neurol*. 66(3):343–348.
24 Feringa FM, van der Kant R. 2021. Cholesterol and Alzheimer's disease; from risk genes to pathological effects. *Front Aging Neurosci*. 13:690372.
25 Nadezhdin KD, Bocharova OV, Bocharov EV, Arseniev AS. 2011. Structural and dynamic study of the transmembrane domain of the amyloid precursor protein. *Acta Nat*. 3(1):69–76.
26 Barrett P, *et al.* 2012. The amyloid precursor protein has a flexible transmembrane domain and binds cholesterol. *Science*. 336: 1168–1171.
27 Hutchison JM, *et al.* 2020. Bicelles rich in both sphingolipids and cholesterol and their use in studies of membrane proteins. *J Am Chem Soc*. 142(29):12715–12729.

28 Song Y, Hustedt EJ, Brandon S, Sanders CR. 2013. Competition between homodimerization and cholesterol binding to the C99 domain of the amyloid precursor protein. *Biochemistry*. 52(30): 5051–5064.

29 Lemmin T, Dimitrov M, Fraering PC, Dal Peraro M. 2014. Perturbations of the straight transmembrane α-helical structure of the amyloid precursor protein affect its processing by γ-secretase. *J Biol Chem*. 289(10):6763–6774.

30 Chiang Y-W, Zheng T-Y, Kao C-J, Horng J-C. 2009. Determination of interspin distance distributions by cw-ESR is a single linear inverse problem. *Biophys J*. 97(3):930–936.

31 Bottorf L, Rafferty S, Sahu ID, McCarrick RM, Lorigan GA. 2017. Utilizing electron spin echo envelope modulation to distinguish between the local secondary structures of an α-helix and an amphipathic 3_{10}-helical peptide. *J Phys Chem B*. 121(14): 2961–2967.

32 Gallová J, Uhríková D, Islamov A, Kuklin A, Balgavý P. 2004. Effect of cholesterol on the bilayer thickness in unilamellar extruded DLPC and DOPC liposomes: SANS contrast variation study. *Gen Physiol Biophys*. 23(1):113–128.

33 Hung W-C, Lee M-T, Chen F-Y, Huang HW. 2007. The condensing effect of cholesterol in lipid bilayers. *Biophys J*. 92:3960–3967.

34 Lin CY, *et al.* 2016. Intranasal administration of a polyethylenimine-conjugated scavenger peptide reduces amyloid-β accumulation in a mouse model of Alzheimer's disease. *J Alzheimers Dis*. 53(3):1053–1067.

35 Shen HC, *et al.* 2019. Segments in the amyloid core that distinguish hamster from mouse prion fibrils. *Neurochem Res*. 44(6): 1399–1409.

36 Chen F-Y, Lee M-T, Huang HW. 2002. Sigmoidal concentration dependence of antimicrobial peptide activities: a case study on alamethicin. *Biophys J*. 82(2):908–914.

37 Georgieva ER, *et al.* 2012. Effect of freezing conditions on distances and their distributions derived from double electron electron resonance (DEER): a study of doubly-spin-labeled T4 lysozyme. *J Magn Reson*. 216:69–77.

38 Sung TC, *et al.* 2015. Solution structure of apoptotic BAX oligomer: oligomerization likely precedes membrane insertion. *Structure*. 23(10):1878–1888.

39 Jeschke G. 2012. DEER Distance measurements on proteins. *Annu Rev Phys Chem*. 63:419–446.

40 Chiang YW, Borbat PP, Freed JH. 2005. The determination of pair distance distributions by pulsed ESR using Tikhonov regularization. *J Magn Reson*. 172(2):279–295.

41 Lai YC, Kuo YH, Chiang YW. 2019. Identifying protein conformational dynamics using spin-label ESR. *Chem Asian J*. 14(22): 3981–3991.

42 Schiemann O, *et al.* 2021. Benchmark test and guidelines for DEER/PELDOR experiments on nitroxide-labeled biomolecules. *J Am Chem Soc*. 143(43):17875–17890.

43 Deligiannakis Y, Louloudi M, Hadjiliadis N. 2000. Electron spin echo envelope modulation (ESEEM) spectroscopy as a tool to investigate the coordination environment of metal centers. *Coord Chem Rev*. 204(1):1–112.

44 Chandrudu S, Simerska P, Toth I. 2013. Chemical methods for peptide and protein production. *Molecules*. 18(4):4373–4388.

45 Zhou A, *et al.* 2012. Determining α-helical and β-sheet secondary structures via pulsed electron spin resonance spectroscopy. *Biochemistry*. 51(38):7417–7419.

46 Chen F-Y, Lee M-T, Huang HW. 2003. Evidence for membrane thinning effect as the mechanism for peptide-induced pore formation. *Biophys J*. 84:3751–3758.

47 Hsieh M-H, *et al.* 2017. Measurement of hanatoxin-induced membrane thinning with lamellar X-ray diffraction. *Langmuir*. 33(11): 2885–2889.

48 Blaurock AE. 1971. Structure of the nerve myelin membrane: proof of the low-resolution profile. *J Mol Biol*. 56(1):35–52.

49 Torbet J, Wilkins M. 1976. X-ray diffraction studies of lecithin bilayers. *J Theor Biol*. 62(2):447–458.

50 Lee M-T, Hung W-C, Chen F-Y, Huang HW. 2008. Mechanism and kinetics of pore formation in membranes by water-soluble amphipathic peptides. *Proc Natl Acad Sci USA*. 105:5087–5092.

51 Wu Y, He K, Ludtke SJ, Huang HW. 1995. X-ray diffraction study of lipid bilayer membranes interacting with amphiphilic helical peptides: diphytanoyl phosphatidylcholine with alamethicin at low concentrations. *Biophys J*. 68(6):2361–2369.